Appl. Math. Mech. -Engl. Ed., **45**(8), 1295–1314 (2024)

APPLIED MATHEMATICS AND MECHANICS (ENGLISH EDITION)

https://doi.org/10.1007/s10483-024-3133-8

On the role of sliding friction effect in nonlinear tri-hybrid vibration-based energy harvesting*

Jiamei WANG[1], Siukai LAI[1,2,†], Chen WANG[3],
Yiting ZHANG[1], Zhaolin CHEN[1,4]

1. Department of Civil and Environmental Engineering, The Hong Kong Polytechnic University, Hong Kong, China;
2. The Hong Kong Polytechnic University Shenzhen Research Institute, Shenzhen 518057, Guangdong Province, China;
3. Hebei Key Laboratory of Mechanical Reliability for Heavy Equipments and Large Structures, Yanshan University, Qinghuangdao 066000, Hebei Province, China;
4. School of Aeronautics, Northwestern Polytechnical University, Xi'an 710072, China

(Received Mar. 12, 2024 / Revised May 31, 2024)

Abstract This work aims to develop an experimental investigation into the effectiveness of the sliding-mode approach for hybrid vibration-based energy harvesting. A proposed sliding-mode triboelectric-electromagnetic-piezoelectric energy harvesting model involves a cantilever beam with a tip mass exposed to magnetic and frictional forces. The experimental findings indicate that the system can achieve its peak inter-well oscillation output within a low-frequency range of 4 Hz–6 Hz. Friction has a lesser impact on the open-circuit voltage output at an excitation acceleration of $1.5g$ compared with $1g$. The distribution of tri-stability changes with the presence of friction. This model provides a deeper understanding of the influence of the dry friction coefficient (0.2–0.5) on the interactive behaviors of different generator units.

Key words sliding mode, tri-hybrid energy harvesting, friction, nonlinear behavior

Chinese Library Classification O322
2010 Mathematics Subject Classification 70K40, 74H45

1 Introduction

Advances in low-power integrated circuits, wireless communications, and mobile electronic technology have led to a growing demand for vibrational energy-harvesting technology in recent decades. Although traditional batteries are widely used as an external power source,

---

* Citation: WANG, J. M., LAI, S. K., WANG, C., ZHANG, Y. T., and CHEN, Z. L. On the role of sliding friction effect in nonlinear tri-hybrid vibration-based energy harvesting. *Applied Mathematics and Mechanics* (*English Edition*), **45**(8), 1295–1314 (2024) https://doi.org/10.1007/s10483-024-3133-8

† Corresponding author, E-mail: sk.lai@polyu.edu.hk

Project supported by the National Natural Science Foundation of China (Nos. 12372024 and 12002300) and the Natural Science Foundation of Hebei Province of China (No. A2021203013)

their limited lifespans and severe environmental effects, coupled with maintenance and replacement issues, underscore the critical need to explore alternative energy sources and develop self-powered systems.

Piezoelectric and electromagnetic working mechanisms have been widely used to design various types of vibration energy harvesters[1–4]. Initially, designers of piezoelectric energy harvesters adopted a cantilever beam model based on linear resonance. However, the drawback of such a model is that it oscillates substantially only at its fundamental resonant frequency, which means that its output decreases markedly with even slight variations in an ambient vibration frequency[5]. In the past two decades, researchers have made significant efforts to enhance the power-generation efficiency of cantilever beam structures, and have reported numerous outstanding advancements that can be used in practical settings. Integrating energy harvesting utilizing electromagnetic, piezoelectric, and triboelectric transduction systems, in particular, has received a great deal of attention[6]. Piezoelectric materials are exceptionally appealing due to their high mechanical-to-electrical energy conversion efficiency and ability to endure significant strain. Besides, unlike electromagnetic harvesters, which are constructed of two separate materials, piezoelectric materials have intrinsic polarization and do not require external aid[7–8]. It implies that piezoelectric material-based energy harvesters are suitable for use in various applications (e.g., transportation monitoring, wireless sensors, and biomedical devices[9–10]).

Piezoelectric materials (e.g., single crystals, ceramics, and polymers) are available in nanostructured forms and thin layers. Some piezoelectric materials such as piezoelectric ceramics and single-crystal materials contain limitations like stringent displacement requirements because of the fragility[11–13]. In this work, a piezoelectric plate is chosen for the design of a cantilever beam with its good performance in transient response of displacement, enabling accurate observation of the structure's motion[14–21]. In contrast to the electromagnetic energy harvester, it is simple and cost-effective with remarkable resistance to damage. From the perspective of energy density, electromagnetic energy harvesters have a lower energy density compared with piezoelectric energy harvesters due to the inherent high density, volume, and weight characteristics of materials[22–23].

The triboelectric nanogenerator (TENG), initially reported in 2012[24], converts mechanical energy into electrical power through a combination of triboelectrification and electrostatic induction. TENG-based energy harvesters offer the benefits of being lightweight, easy to manufacture, and cost-effective, rendering them suitable for a wide range of potential uses. Surface charge density is one of the most critical factors determining the performance of TENG. It can be increased by choosing suitable charging materials and enlarging contact surfaces[25]. Studies on various TENG applications have primarily focused on advances in material surface processing techniques[26–28].

The electrical energy obtained from a single mechanical excitation can be enhanced by combining multiple energy conversion processes, allowing the benefits of different conversion mechanisms to be utilized in a single device[29–36]. This type of integration boosts a device's energy density, broadening the spectrum of its potential uses[29,37]. With the low-frequency vibration excitation considered, various conversion methods have been developed to create structures for resonating. The first piezoelectric-electromagnetic-triboelectric ("tri-hybrid") energy harvester can be traced back to 2017[38], providing inspiration for other researches. Various approaches, including employing impact-driven piezoelectric generators (PEGs)[33], frequency up-conversion mechanism[39], and adding external non-conservative forces[31], have been proposed to enhance output performance under low-excitation conditions.

Unlike piezoelectric and electromagnetic energy harvesters, TENG-driven devices are constructed from readily available materials and exhibit high-voltage and low-current output traits[40–41]. Generally, there are four different working modes, namely a vertical contact-separation mode[42–43], an in-plane sliding mode[44–46], a single-electrode mode[47], and a freestanding triboelectric-layer mode[48]. In the four fundamental working modes of TENG, sliding-mode TENG is an important one[49–50], and this phenomenon is initiated by the relative sliding between triboelectric layers.

Mu et al.[51] fabricated an arrayed contact-separation structure that increased the output performance of a hybrid enhanced TENG by 104%. The latest literature on advances in energy harvesting using micro- and nano-scale generators that exploit piezoelectric and frictional electric effects has been extensively reviewed[52]. Tan et al.[53] conducted a numerical dynamic analysis to examine the sliding-mode friction acting on a bird-shaped cantilever. Fu et al.[54] have devised a sliding-mode triboelectric energy harvester to analyze the effect of friction in terms of structural dynamics and static electricity. Their study is a rare example of an investigation on the dynamics of energy harvesters in relation to frictional forces, making it a valuable contribution to recent literature. The researchers further studied the slip-stick behavior to determine the effect of friction on energy-harvesting efficiency[55]. Despite the presentation of analytical models in the previous studies, the investigation into the friction effect of multi-stable systems and its mechanism is still scarce. In addition, experimental conditions, such as humidity, temperature, spillage of material, and the process used to fabricate a prototype affect the friction coefficient and energy-harvesting performance of a device[56–58]. Despite numerous numerical studies that have been conducted, there remains a need for practical experimental investigations on sliding-mode triboelectric energy harvesters. In most hybrid harvesting structures, the inclusion of friction is essential[59] and poses a significant challenge when attempting to isolate its effects. Therefore, it is crucial to design a comprehensive model that concurrently investigates the influence of friction on the dynamics aspect by analyzing both simulation and experimental data.

This work proposes a simple model in the form of a cantilever structure with a tip mass to evaluate the effect of frictional force on tri-hybrid energy harvesting. The main contributions of this study are as follows:

(i) A structural dynamics approach is adopted to model and investigate a triboelectric energy harvester with sliding-mode operation. Different types of stability resulting from a magnetic field are identified by using the magnetizing current method for force calculations.

(ii) The effect of the friction coefficient on the dynamics of the entire structure is investigated through numerical simulations.

(iii) The multi-stability dynamics of the model is examined through an experimental approach, with a primary emphasis on the impact of a non-conservative force (friction) at low frequencies ranging from 2 Hz to 8 Hz.

The remainder of this paper is organized as follows. Section 2 introduces the design of a harvester, describes its working mechanism, and presents the preliminary testing and experimental setup. Section 3 presents the experimental and simulation results. Section 4 summarizes the findings of this study.

2 Structural design and working mechanism

2.1 Structural configuration

The configuration of the tri-hybrid vibration-based energy harvesting model is presented in Fig. 1(a). All of the generator units are integrated onto a base that is embedded on a vibration shaker, which is controlled by a power amplifier. The PEG unit has a copper cantilever beam that is clamped onto the base. Two macro fiber composite (MFC) patches (MFC-2807-P2) are mounted on the beam. These two MFC patches and the surfaces on both sides of the adhered copper beam constitute PEG1 and PEG2 units, respectively. Magnet A is attached to the free end of the beam, while the external magnets (B and C) are positioned symmetrically on the base to create a restoring force. The dimensions of the beryllium bronze beam are 89 mm × 12 mm × 0.25 mm, the two external magnets (i.e., Magnets B and C) have dimensions of 7.5 mm × 9.5 mm × 1.5 mm, and Magnet A has dimensions of 9.8 mm × 9.8 mm × 4 mm. The electromagnetic generator (EMG) unit comprises Magnet A and four copper coils. The four coils are placed between the external magnets and Magnet A, and they are labeled 1, 2, 3, and 4, as shown in Fig. 1; Coil 1 is symmetric about Coil 4, and Coil 2 is symmetric about Coil 3. Coils 1 and 4 are connected in series (i.e., "EMG1"), while Coils 2 and 3 are connected in series (i.e., "EMG2"). The sliding contact area of the TENG unit is a printed circuit board with an 80-µm polytetrafluoroethylene (PTFE) film coating, interdigitated parallel copper electrodes, and a glass epoxy base. A rectangular resin plate with parallel arrayed copper electrodes is fixed onto the bottom of Magnet A. The schematic diagram of the preset positions of the three magnets is shown in Fig. 1(b). The center points of the magnets are denoted as A, B, and C, respectively. The separation of Magnets B and C is denoted as f, and the horizontal magnet interval between Point A and the BC-plane is denoted as d. In Table 1, the governing parameters are presented.

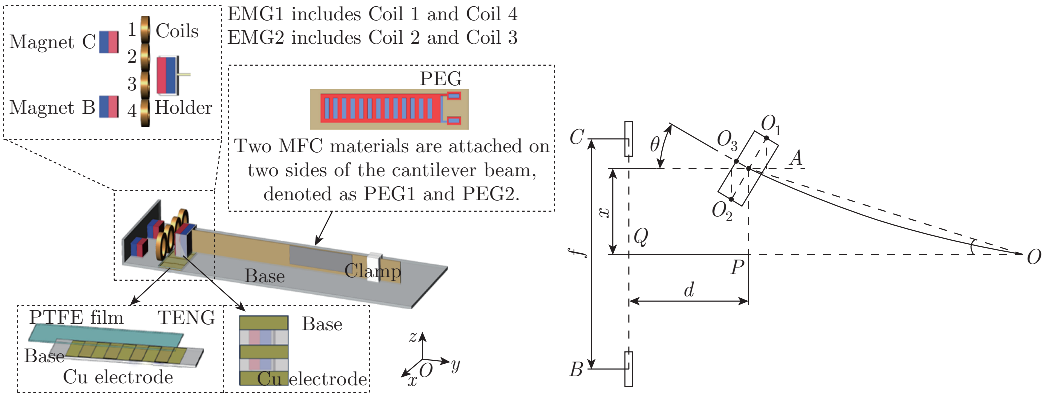

(a) (b)

Fig. 1 (a) Schematic of the tri-hybrid energy harvesting model; (b) schematic of the preset positions of Magnets A, B, and C (color online)

Table 1 Material parameters of the tri-hybrid energy harvesting model

Item	Parameter	Value
Cantilever beam	Length (L_b) × width (W_b) × thickness (T_b)	89 mm × 12 mm × 0.25 mm
	Elasticity modulus (E_b)	100 GPa
	Density (ρ_b)	7 765 kg/m^3
MFC patch	Length (L_p) × width (W_p) × thickness (T_p)	37 mm × 10 mm × 0.27 mm
	Elasticity modulus (E_p)	100 GPa
	Density (ρ_p)	5.44 g/cm^3
Magnet	Piezoelectric constant (d_{31})	−190 pC/N
	Dimensions of Magnet A	9.8 mm × 9.8 mm × 4 mm
	Dimensions of Magnets B and C	7.5 mm × 9.5 mm × 1.5 mm
	Density (ρ_A, ρ_B, and ρ_C)	7 500 kg/m^3
	Magnetization (M_A, M_B, and M_C)	7.4×10^{-5} A/m
Four copper coil	Length × width × thickness	12 mm × 16.5 mm × 3 mm
	Number of turns	650
TENG unit	PTFE: length × width × thickness	60 mm × 12.5 mm × 0.35 mm
	Copper film thickness	0.02 mm

When Magnet A oscillates due to the base acceleration, its motion is affected by the restoring force generated by the external magnets (B and C). Triboelectrification occurs in the contact area due to the motion of Magnet A (i.e., copper electrodes) relative to the negatively charged triboelectric material (i.e., PTFE film). That is, during relative sliding motion, the copper electrodes (at the bottom of Magnet A) are positively charged, whereas the PTFE film is negatively charged. The resulting electrostatic equilibrium means that there is no charge transfer between the copper electrodes and PTFE film during the movement. As Magnet A moves, electrons flow from the top electrode to the bottom electrode, resulting in current flowing in the opposite direction. The process repeats as the slider oscillates and represents a half cycle of the TENG unit. The mechanisms of many harvesters have rarely been studied because of dry friction between the tip magnet and base. It is found that this hybrid tri-stable energy harvesting model exhibits better performance than the traditional bi-stable or tri-stable cantilever beam harvesting models.

2.2 Theoretical model and working mechanism

The equations for modeling the mechanical system in Fig. 1 can be derived using the Lagrange-D'Alembert principle and Hamilton principle[60] in the presence of external forces, such as a frictional force[61]. The general form of the equation for the mechanical system is

$$\int_{t_1}^{t_2} (\delta(T-U)+\delta W)\mathrm{d}t = 0, \tag{1}$$

where T and U are the kinetic energy and potential energy of the system, respectively; t_1 and t_2 are the initial time and final time, respectively; W is the kinetic energy resulting from the nonconservative (frictional) force, and

$$W = \int_0^{L_\mathrm{b}} F_\mathrm{f}\delta(x-L_\mathrm{b})w(x,t)\mathrm{d}x, \tag{2}$$

where L_b is the length of the cantilever beam, F_f is the nonconservative force (friction force), $\delta(x-L_\mathrm{b})$ is the Dirac delta function, and $w(x,t)$ is the deflection of the beam relative to the base. The kinetic energy of the cantilever beam and piezoelectric layers is given by

$$T_{\mathrm{b+p}} = \frac{1}{2}\rho_\mathrm{b}A_\mathrm{b}\int_0^{L_\mathrm{b}} \Big(\frac{\partial w(x,t)}{\partial t}+\frac{\partial b(t)}{\partial t}\Big)^2\mathrm{d}x + \frac{1}{2}\rho_\mathrm{p}A_\mathrm{p}\int_0^{L_\mathrm{p}} \Big(\frac{\partial w(x,t)}{\partial t}+\frac{\partial b(t)}{\partial t}\Big)^2, \tag{3}$$

where ρ_b and A_b are the density and cross-sectional area of the cantilever, respectively; ρ_p, A_p, and L_p are the density, cross-sectional area, and length of the piezoelectric layers, respectively; $b(t)$ is the base displacement. The kinetic energy of Magnet A (tip magnet) is

$$T_\mathrm{m} = \frac{1}{2}m\Big(\frac{\partial w(x,t)}{\partial t}+\frac{\partial b(t)}{\partial t}\Big)^2_{x=L_\mathrm{b}}, \tag{4}$$

where m is the mass of Magnet A. In general, the moment of inertia should be considered. However, in this design, the moment of inertia is deemed insignificant due to the low mass of the tip of Magnet A. The total kinetic energy T can be obtained from Eqs. (3) and (4).

The potential energy of the cantilever beam with piezoelectric layers is given by

$$U_{\mathrm{b+p}} = \frac{1}{2}E_\mathrm{b}I_\mathrm{b}\int_0^{L_\mathrm{b}} \Big(\frac{\partial^2 w(x,t)}{\partial x^2}\Big)^2\mathrm{d}x + E_\mathrm{p}I_\mathrm{p}\int_0^{L_\mathrm{p}} \Big(\frac{\partial^2 w(x,t)}{\partial x^2}\Big)^2\mathrm{d}x, \tag{5}$$

where E_b and E_p are Young's moduli of the beam and the MFC layers, respectively; I_b and I_p are the area moments of inertia of the beam and the MFC layers, respectively. The elastic potential energy provided by the magnetic field is given by

$$U_\mathrm{m} = \int F_x\mathrm{d}w, \tag{6}$$

where F_x denotes the total magnetic force.

A three-dimensional reference system is established for the structure. Magnet A is fixed on the top of the copper beam, which is placed on the xy-plane and moves along the x-axis. A magnetizing current method[62] is adopted in the current magnet model. Magnetic forces generated by the two external fixed magnets ($\boldsymbol{F}_{\text{B-}x}$ and $\boldsymbol{F}_{\text{C-}x}$) act on Magnet A to move it in the x-direction. In addition, Magnets B and C generate magnetic forces in the x-direction. $\boldsymbol{F}_{\text{B-}x}$ and $\boldsymbol{F}_{\text{C-}x}$ are written as follows:

$$\begin{cases} \boldsymbol{F}_{\text{B-}x} = \displaystyle\iint_S \boldsymbol{K}_{\text{m}} \times \boldsymbol{B}_{\text{ext-B}} \mathrm{d}S, \\ \boldsymbol{F}_{\text{C-}x} = \displaystyle\iint_S \boldsymbol{K}_{\text{m}} \times \boldsymbol{B}_{\text{ext-C}} \mathrm{d}S, \end{cases} \tag{7}$$

where $\boldsymbol{K}_{\text{m}}$ is the surface current density of Magnet A; $\boldsymbol{B}_{\text{ext-B}}$ and $\boldsymbol{B}_{\text{ext-C}}$ are the external magnetic flux densities of Magnets B and C, respectively; S is the surface area of Magnet A. $\boldsymbol{K}_{\text{m}}$ is given by

$$\boldsymbol{K}_{\text{m}} = \boldsymbol{m}_{\text{A}} \times \boldsymbol{n}, \tag{8}$$

where $\boldsymbol{m}_{\text{A}}$ is the magnetization of Magnet A, and $\boldsymbol{n}$ is the unit vector in the direction outward from the surface. The magnetizing current densities on the top and bottom surfaces of Magnet A can be ignored, owing to the magnetization $\boldsymbol{K}_{\text{m}}$ of Magnet A being in the x-direction. The magnet flux density of an isotropic medium is expressed as follows:

$$\boldsymbol{B} = \mu_0 \boldsymbol{H}, \tag{9}$$

where μ_0 is the permeability, and $\boldsymbol{H}$ is the magnetic field strength. In this work, we only consider the x-direction in adopting the magnetizing current method with calculation of the magnetic forces, that is,

$$F_x = \mu_0 M_{\text{A}} S (H_{y1} - H_{y2}), \tag{10}$$

where M_{A} is the magnitude of magnetization of Magnet A; H_{y1} and H_{y2} are the magnitudes of the magnetic field intensity in the y-direction at the centers of the front and back surfaces of Magnet A, respectively.

The magnetic field strength at the point (x, y, z) in the y-direction is written as[63]

$$\begin{aligned} H_y(x,y,z) = \frac{M_{\text{C}}}{4\pi} \Big(& \arctan\Big(\frac{x_{\text{p}} z_{\text{p}}}{y\sqrt{x_{\text{p}}^2 + z_{\text{p}}^2 + y^2}}\Big) + \arctan\Big(\frac{x_{\text{n}} z_{\text{n}}}{y\sqrt{x_{\text{n}}^2 + z_{\text{n}}^2 + y^2}}\Big) \\ & - \arctan\Big(\frac{x_{\text{n}} z_{\text{p}}}{y\sqrt{x_{\text{n}}^2 + z_{\text{p}}^2 + y^2}}\Big) - \arctan\Big(\frac{x_{\text{p}} z_{\text{n}}}{y\sqrt{x_{\text{p}}^2 + z_{\text{n}}^2 + y^2}}\Big)\Big), \end{aligned} \tag{11}$$

where $x_{\text{p}} = x + l_{\text{C}}/2$, $x_{\text{n}} = x - l_{\text{C}}/2$, $z_{\text{p}} = z + w_{\text{C}}/2$, and $z_{\text{p}} = z - w_{\text{C}}/2$, in which l_{C} and w_{C} are the length in the x-direction and width in the z-direction of Magnet C, respectively. M_{C} is the magnitude of magnetization of Magnet C. The magnetic force generated by Magnets B and C and acting on Magnet A in the x-direction is

$$F_x = \mu_0 M_{\text{A}} S (H_{\text{B-}y1} - H_{\text{B-}y2} + H_{\text{C-}y1} - H_{\text{C-}y2}), \tag{12}$$

where $H_{\text{B-}y1}$ and $H_{\text{B-}y2}$ are the magnitudes of the magnetic field intensity in the y-direction generated by Magnet B at the centers of the front and back surfaces of Magnet A, respectively. $H_{\text{C-}y1}$ and $H_{\text{C-}y2}$ are the magnitudes of the magnetic field in the y-direction generated by Magnet C at the centers of the front and back surfaces of Magnet A, respectively.

By setting the coordinate origin at the center of Magnet C and taking into account the arc-shaped trajectory of the tip magnet's movement, we find that the spatial coordinates of the points O_1 and O_2 are, respectively, expressed as follows:

$$(f/2 - x - l_{\mathrm{A}}/2 \times \cos\theta, d + l_{\mathrm{A}} \times (1 - \cos\theta) + w_{\mathrm{A}}/2 \times \sin\theta, 0), \tag{13a}$$

$$(f/2 - x + l_{\mathrm{A}}/2 \times \cos\theta, d + l_{\mathrm{A}} \times (1 - \cos\theta) - w_{\mathrm{A}}/2 \times \sin\theta, 0), \tag{13b}$$

where θ is the angle between AO_3 and the horizontal direction (see Fig. 1(b)); l_{A} and w_{A} are the length and width of Magnet A, respectively. Similarly, setting the coordinate origin at the center of Magnet B, we find that the spatial coordinates of the points O_1 and O_2 are, respectively, written as

$$(-f/2 - x - w_{\mathrm{A}}/2 \times \cos\theta, d + l_{\mathrm{A}} \times (1 - \cos\theta) + w_{\mathrm{A}}/2 \times \sin\theta, 0), \tag{14a}$$

$$(-f/2 - x + w_{\mathrm{A}}/2 \times \cos\theta, d + l_{\mathrm{A}} \times (1 - \cos\theta) - w_{\mathrm{A}}/2 \times \sin\theta, 0). \tag{14b}$$

The cantilever beam is assumed to be a uniform Euler-Bernoulli beam, and the transverse displacement of the beam is approximated as follows:

$$w(x,t) = \phi(x)q(t), \tag{15}$$

where $q(t)$ denotes the associated time-varying generalized coordinate, and $\phi(x)$ is the mode shape function. In this work, we only consider the first-order mode as this is a dominant vibration mode. The latter is obtained by solving the eigenvalue problem for the first-order mode of an undamped and linearized cantilever beam with a tip magnet, that is,

$$\phi(x) = C_1\Big(\Big(\cos\Big(\frac{\lambda}{L}x\Big) - \cosh\Big(\frac{\lambda}{L}x\Big)\Big) + \sigma\Big(\sin\Big(\frac{\lambda}{L}x\Big) - \sinh\Big(\frac{\lambda}{L}x\Big)\Big)\Big), \tag{16}$$

where C_1 is an arbitrary amplitude that is derived from the corresponding orthonormality conditions (with the corresponding formulas not given here), and σ and λ are determined from the associated eigensystem. We substitute Eq. (15) into the previously mentioned potential (Eqs. (3) and (4)) and kinetic (Eqs. (5) and (6)) energy formulas, and then apply the resulting equations to Eq. (17). A Lagrange function can be derived for the entire system using modal coordinates and a mode shape function.

On the basis of the D'Alembert principle, which is equivalent to the Euler-Lagrange equations with external forces, the governing equation of the mechanical system is

$$\frac{\mathrm{d}}{\mathrm{d}t}\Big(\frac{\partial L}{\partial \dot{q}}\Big) - \frac{\partial L}{\partial q} = F_{\mathrm{f}}\phi(L_{\mathrm{b}}), \tag{17}$$

where $L = T - U$ with T and U being the kinetic energy and the potential energy of the system, respectively. F_{f} is the kinetic frictional force acting on the tip magnet, given by

$$F_{\mathrm{f}} = -\mu m g \,\mathrm{sgn}(\dot{q}\phi(L_{\mathrm{b}})), \tag{18}$$

where μ is the friction coefficient, m is the mass of Magnet A, g is the acceleration of gravity, and $\mathrm{sgn}(\cdot)$ is the signum function. Through applying the orthonormality conditions and including damping, we have

$$\ddot{q} + 2\varsigma\omega\dot{q} + \omega^2 q - \theta v = \alpha\ddot{b} + F_{\mathrm{f}}\phi(L_{\mathrm{b}}) + F_x\phi(L_{\mathrm{b}}), \tag{19}$$

where ς is the damping ratio; ω is the undamped natural frequency of the first mode of the beam without the tip mass; $\ddot{b}$ is the base acceleration; F_x is the magnetic force exerted by the magnetic field at the tip.

2.3 Experimental setup

Figure 2(a) shows the experimental setup. Harmonic excitations were generated by a vibration exciter (SPEKTRA APS 113). The model was fixed on the shaking table using a screw link. A signal generator (Keysight 33500B) and power amplifier (APS 125) were used to generate excitation signals. Acceleration and frequency data were recorded using an accelerometer (Dytran 3023A3H), which was connected to a data acquisition system (Dewesoft SIRIUSi-8xACC), and observed on a computer equipped with bundled software. The output voltage data were recorded using an oscilloscope (Keysight DSOX3014T).

Based on the schematic model, a preliminary test and numerical simulation needed to be conducted before the analysis of the output experimental results. First, the restoring force was measured to obtain the magnet spacings (i.e., f and d, as indicated in Fig. 1(b)), which greatly affected the steady state and output of the structure. A digital dynamometer and micrometer were used to measure the forces acting on the magnetic slider under different displacements, as shown in Fig. 2(b). Figure 2(c) shows the three stable positions of the beam with the tip magnet under an external magnetic force, which correspond to two symmetric static equilibria and one central static equilibrium. Magnet spacings (d and f) needed to be adjusted until the tri-stable state was achieved.

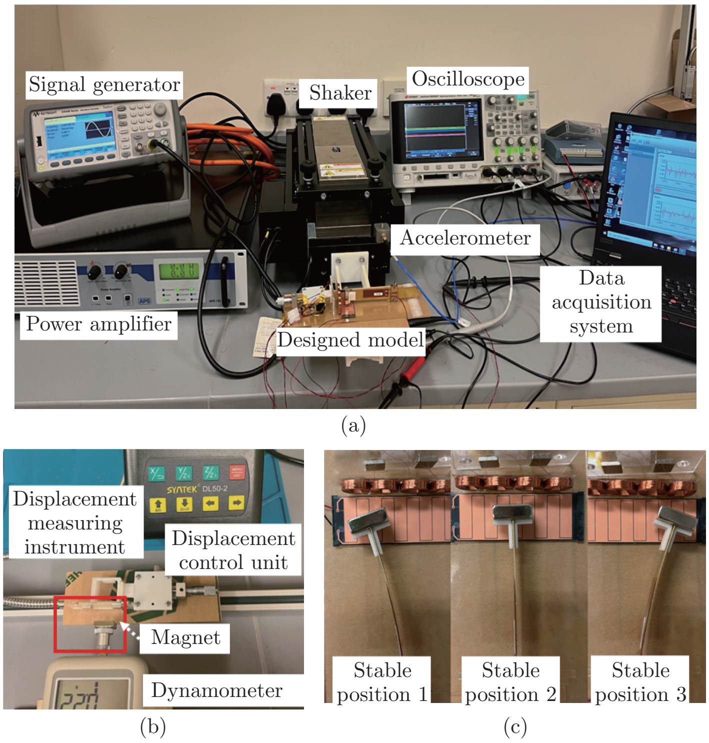

Fig. 2 (a) Experimental setup; (b) magnetic force measurement; (c) three equilibrium points (color online)

Figure 3(a) shows the magnetic force F_{m} calculation and results of tests of energy harvesters with two different tri-stable modes (the first one: $d = 12.5\,\mathrm{mm}$, and $f = 17\,\mathrm{mm}$; the second one: $d = 14.5\,\mathrm{mm}$, and $f = 17\,\mathrm{mm}$). The results obtained using the above method for calculating the magnetic force are almost identical to the experimental test results. The two calculated restoring force results which consist of the magnetic force and elastic force of the beam are shown in Fig. 3(b). After confirming the feasibility of the calculation method, a potential energy analysis is carried out as shown in Fig. 3(c) for $d = 12.5\,\text{mm}$. Compared with a higher excitation frequency, it is found that a lower excitation frequency is preferable for the nonlinear system, due to the shadow depth of the potential well. Consequently, the output performance of the PEG unit is improved under low-frequency and low-intensity vibrations. The frequency responses of the PEG, EMG, and TENG units under various base accelerations ($0.5g$, $1g$, and $1.5g$) are investigated in the next section. Peak-to-peak (P-P) open-circuit voltage levels are experimentally measured in a frequency range of 2 Hz–8 Hz.

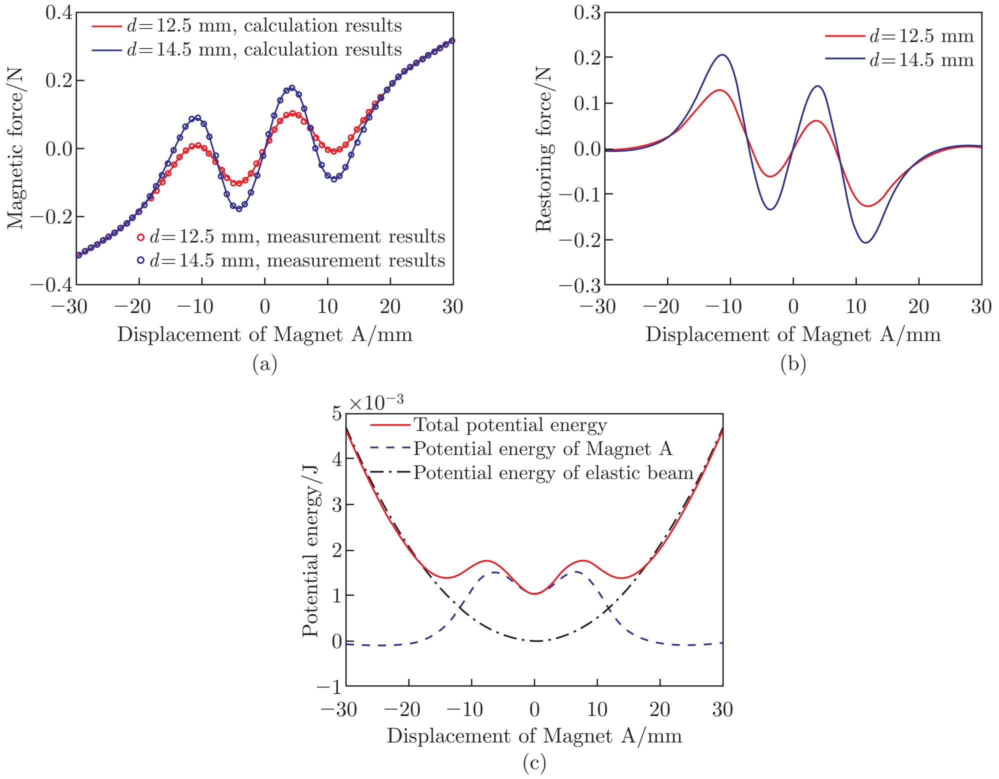

(a) (b) (c)

Fig. 3 (a) Calculation and measurement results of the magnetic force for $d = 12.5\,\text{mm}$ and $d = 14.5\,\text{mm}$; (b) the restoring force of Magnet A for $d = 12.5\,\text{mm}$ and $d = 14.5\,\text{mm}$; (c) the total potential energy of Magnet A and elastic beam (color online)

3 Results and discussion

3.1 Simulation results

Numerical simulations are indispensable for fully validating the dynamic effect of friction on multi-stable nonlinear structures. In energy harvesting systems, the intricate relationship between friction and output is increased by the diverse arrangements of frictional materials. From the perspective of material characteristics, the coefficient of friction is highly correlated to various factors such as external load (normal load), sliding speed, contact temperature, friction time, and curing temperature. It implies that the coefficient of friction is hard to be identified as a precise value, because it may change with time and the surrounding environment.

In this study, we can calculate the external load of Magnet A: $F_{\text{nA}} = \rho_{\text{A}} \times V_{\text{A}} \times g = 0.028\,24\,\text{N}$, and the pressure provided by Magnet A is $P_{\text{A}} = F_{\text{nA}}/S = 720\,\text{Pa}$, where S is the lower surface (contact surface) area. Based on the analysis of the previous works[55–58], it can be inferred that the range of coefficients falls within approximately 0.3 based on F_{nA} and P_{A} at $1g$ and $1.5g$ accelerations. To observe the effect of frictional forces, we thus set μ from 0.2 to 0.5 in the numerical simulations. Figure 4 illustrates the tip vibration amplitudes during a frequency sweeping process of up-conversion (from 1 Hz to 15 Hz) and down-conversion (from 15 Hz to 1 Hz) for $\mu \in [0.2, 0.5]$, at two different initial phases (i.e., $y_{\mathrm{initial}} = 4\,\mathrm{mm}$, $20\,\mathrm{mm}$). The initial state of the structure exerts a significant effect on the dynamic analysis. An increase in the friction coefficient (μ) results in the decreased vibration amplitudes, leading to the reduced inter-well motion, fewer tri-stable states, yet more monostable and bistable states. In the absence of frictional effects, the inter-trap motion becomes more stable. Under the given excitation, the presence of tri-stable states becomes more pronounced, facilitating inter-well transitions. This finding provides further evidence for the detrimental effect of friction on the output.

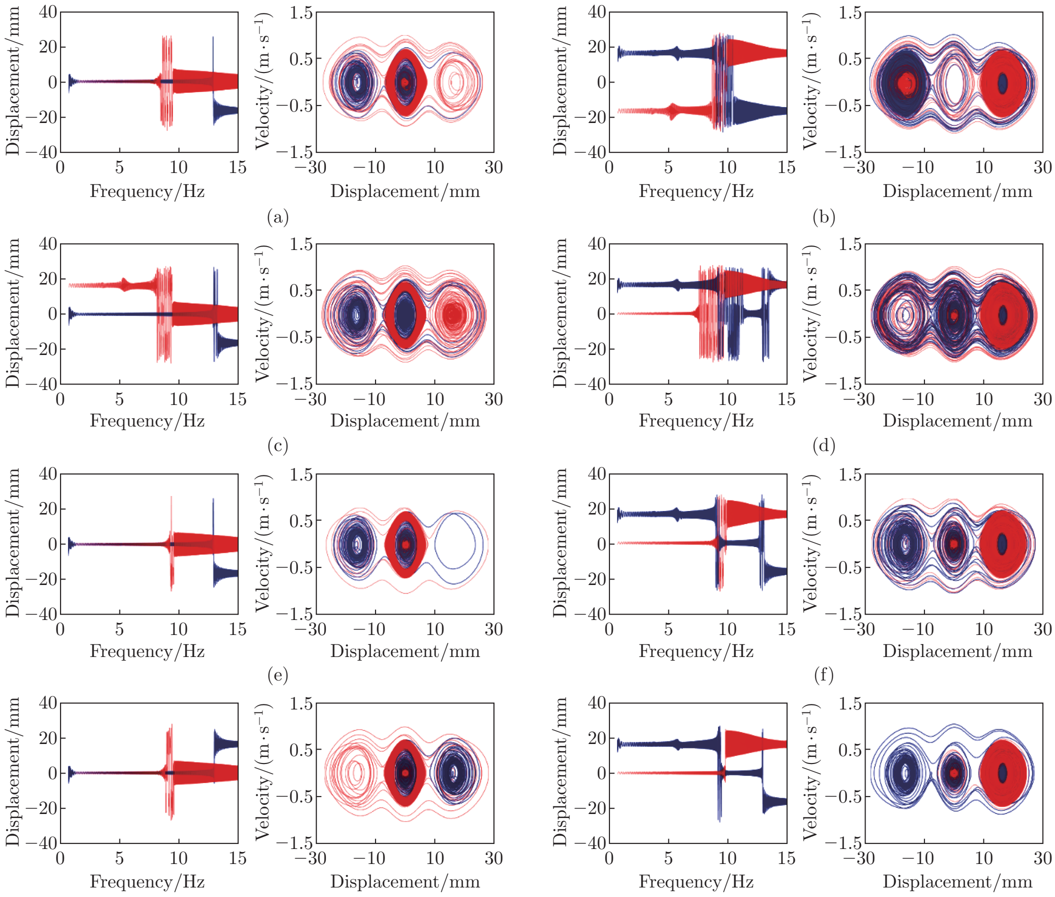

(a) (b) (c) (d) (e) (f) (g) (h)

Fig. 4 Time-domain analysis of tip magnet vibration amplitudes and phase portraits at an excitation acceleration of $1g$: (a) $\mu = 0.2$, $y_{\mathrm{initial}} = 4\,\mathrm{mm}$; (b) $\mu = 0.2$, $y_{\mathrm{initial}} = 20\,\mathrm{mm}$; (c) $\mu = 0.3$, $y_{\mathrm{initial}} = 4\,\mathrm{mm}$; (d) $\mu = 0.3$, $y_{\mathrm{initial}} = 20\,\mathrm{mm}$; (e) $\mu = 0.4$, $y_{\mathrm{initial}} = 4\,\mathrm{mm}$; (f) $\mu = 0.4$, $y_{\mathrm{initial}} = 20\,\mathrm{mm}$; (g) $\mu = 0.5$, $y_{\mathrm{initial}} = 4\,\mathrm{mm}$; (h) $\mu = 0.5$, $y_{\mathrm{initial}} = 20\,\mathrm{mm}$, where blue lines represent up-conversion frequency sweeping results, while red lines represent down-conversion frequency sweeping results (color online)

At an excitation acceleration of $1g$ and a frequency of 2 Hz, owing to the effect of the frictional force, the dynamic properties of the tip magnet transition from multi-stable states to a monostable state, as shown in Fig. 5. It is found that as the excitation level decreases, there is a reduction in the frequency bandwidth of inter-well oscillations. In addition, the amplitude decreases. The outputs of the piezoelectric material (MFC plates) positively correlate with the displacement of the tip magnet. Figure 6 shows that at an excitation acceleration of $1g$ and a frequency of 5 Hz, owing to the effect of friction, there is a slight decrease in the amplitude without a substantial change in stability. Figure 7 illustrates that, at an excitation acceleration of $1.5g$ and a frequency of 5 Hz, the displacement of the tip magnet is slightly constrained by friction, leading to a marginal reduction in the inter-trap motion bandwidth. Nonetheless, the system still exhibits a tri-stable state. When the excitation is high (see Figs. 7(a) and 7(b)), friction has a relatively minor impact compared with that for a low excitation (see Figs. 5(a) and 5(b)). The overall trends of Figs. 6(a) and 6(b) are similar to those of Figs. 7(a) and 7(b). However, due to a higher acceleration excitation, a larger displacement is observed in Fig. 7.

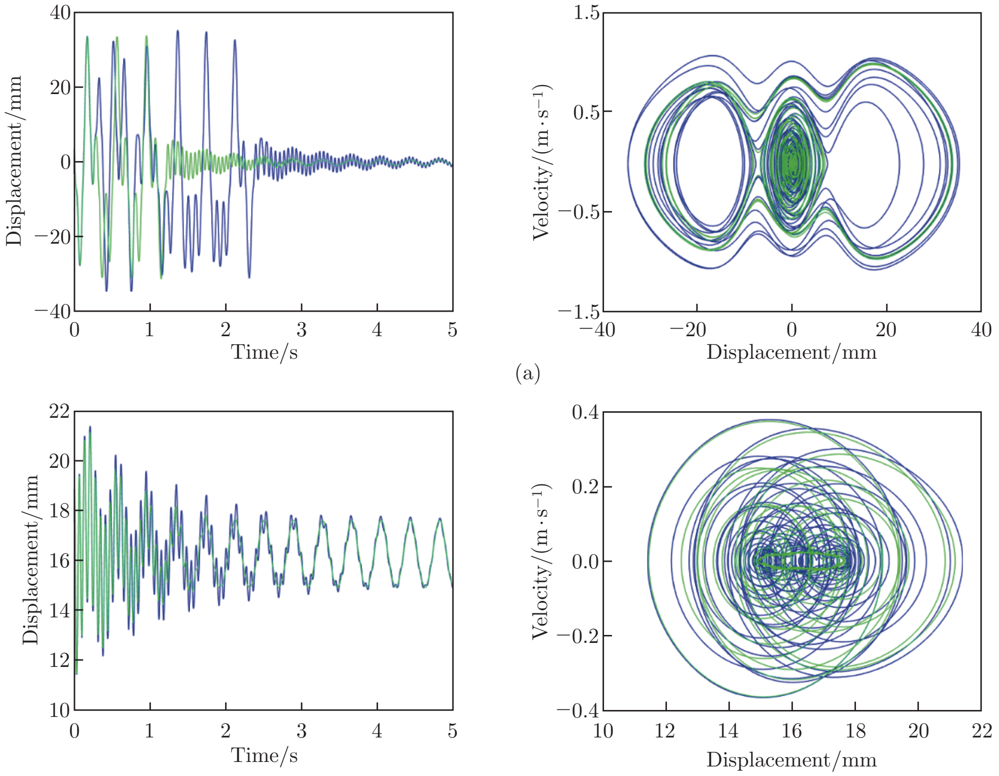

(a)

(b)

Fig. 5 Phase diagrams for the dynamic motion of Magnet A: (a) $y_{\text{initial}} = 4$ mm and (b) $y_{\text{initial}} = 20$ mm without and with friction at an excitation acceleration of $1g$ and a frequency of 2 Hz, where blue lines represent the results without friction, while green lines represent the results with friction ($\mu = 0.3$) (color online)

3.2 Experimental results

Owing to friction, the tip of Magnet A struggles to produce an efficient output at an excitation acceleration of $0.5g$, and thus no measurements are made on the PEG and EMG units under the effect of the TENG at an excitation acceleration of less than $0.5g$. In addition, at an excitation acceleration of $0.5g$, it is difficult for the tip magnet to move between wells, and the measurement range is thus from 2 Hz to 8 Hz. As all of the harvester units in the prototype are driven by identical mechanical motions, their open-circuit voltages have similar broadband responses based on the selected multi-stable nonlinearity mode. In addition, owing to symmetry, the opposite side of the beam theoretically should have produced an equivalent output.

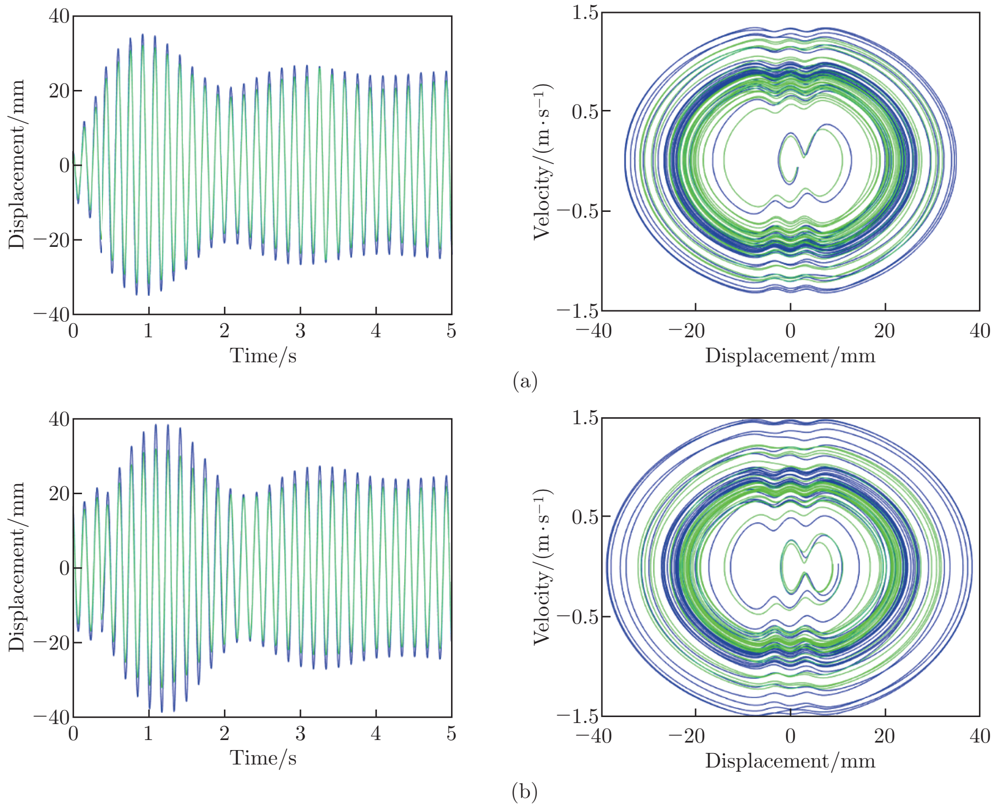

Fig. 6 Phase diagrams for the dynamic motion of Magnet A: (a) $y_{\text{initial}} = 4\,\text{mm}$ and (b) $y_{\text{initial}} = 20\,\text{mm}$ without and with friction at an excitation acceleration of $1g$ and a frequency of 5 Hz, where blue lines denote the results without friction, while green lines denote the results with friction ($\mu = 0.3$) (color online)

However, to ensure experimental accuracy, comparative tests are conducted on the symmetric elements. In the following, we investigate the presence and absence of the sliding-mode friction effect, i.e., with and without the TENG unit.

The experimental open-circuit voltage P-P values of two PEG units (with two sides) at 2 Hz–8 Hz are presented in Fig. 8(a). The PEG unit exhibits a higher output under conditions of high acceleration compared with that under low acceleration. As the acceleration increases, the maximum response frequency gradually increases and then rapidly declines. As the input frequency increases, the slider exhibits large-amplitude inter-well oscillations, leading to high-voltage responses. The maximum single-side PEG unit's output is about 90 V at an excitation acceleration of $1.5g$ and a frequency of 6 Hz–7 Hz. It is noted that the tip magnet struggles to achieve inter-well motion when it is subject to the 2 Hz excitation and $1.5g$ acceleration. Hence, the experimental data are recorded from 3 Hz to 8 Hz in the case of $1.5g$. Moreover, PEG1 and PEG2 data are essentially consistent, indicating that the experimental structure is symmetrical, and thus only PEG2 data are used for comparison in subsequent studies.

The voltage outputs of EMG1 and EMG2 under different excitations ($0.5g$, $1g$, and $1.5g$) are presented in Fig. 8(b). EMG1 comprises two coils located on the outer side, whereas EMG2 comprises two coils located at the center. Regardless of the excitation applied, the output of EMG2 surpasses that of EMG1, owing to a more rapid change in the magnetic field intensity at the center than that on the outer side. The output trends of EMG2 and EMG1 exhibit similarity, demonstrating an ascending pattern at lower frequencies (2 Hz–4 Hz), a smoother

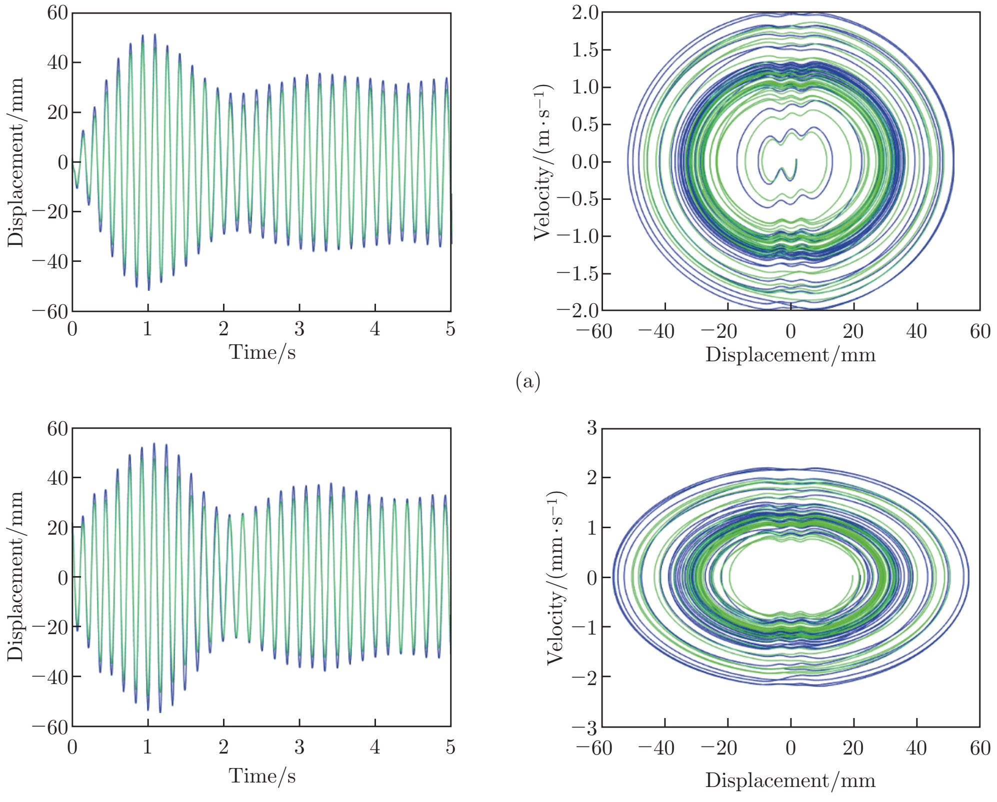

(a)

(b)

Fig. 7 Phase diagrams for the dynamic motion of Magnet A: (a) $y_{\mathrm{initial}} = 4\,\mathrm{mm}$ and (b) $y_{\mathrm{initial}} = 20\,\mathrm{mm}$ without and with friction at an excitation acceleration of $1.5g$ and a frequency of 5 Hz, where blue lines represent the results without friction, while green lines represent the results with friction ($\mu = 0.3$) (color online)

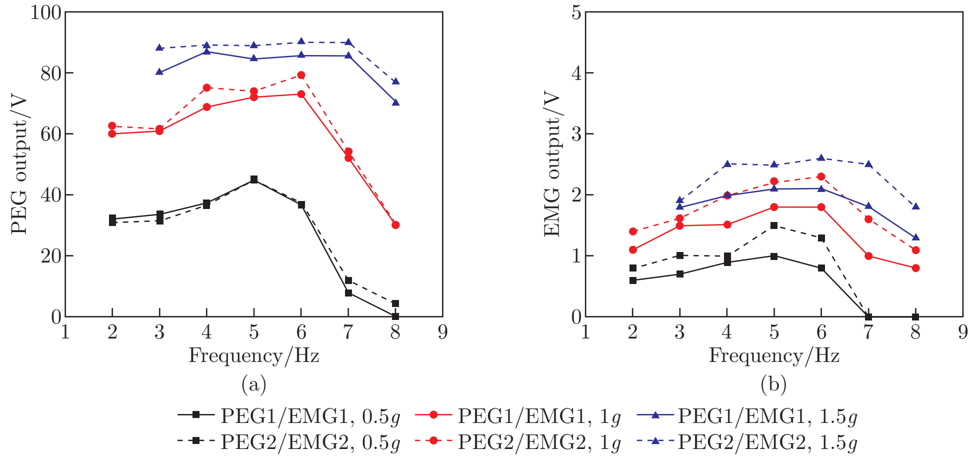

(a)

(b)

Fig. 8 Open-circuit voltage outputs of PEG and EMG at $0.5g$, $1g$, and $1.5g$: (a) PEG1 and PEG2 outputs; (b) EMG1 and EMG2 outputs (color online) trajectory at 5 Hz–6 Hz, and a declining trend after 6 Hz or 7 Hz. The maximum open-circuit voltage output of EMG2 is about 2.6 V at an excitation acceleration of $1.5g$ and a frequency of 6 Hz.

The TENG unit reduces the PEG2 P-P output. This phenomenon may be attributed to the frictional force, which increases the damping factor and restricts beam movement to some extent, resulting in a reduced voltage output. The experimental open-circuit voltage P-P values of PEG2 in a frequency range of 2 Hz–8 Hz in the presence and absence of the TENG are presented in Fig. 9(a). Owing to the effect of friction at an excitation acceleration of $0.5g$, the open-circuit P-P voltage output of PEG2 approaches zero. Therefore, only results for excitation accelerations of $1g$ and $1.5g$ are presented. The figure reveals that friction does not always impede the movement of Magnet A at the beam's tip. At an excitation acceleration of $1g$ and a frequency of 4 Hz, the P-P voltage in the presence of friction exceeds that in the absence of friction, whereas at an excitation acceleration of $1g$ and a frequency of 5 Hz, friction appears to have no effect. At other excitation frequencies, friction has a detrimental effect. At an excitation acceleration of $1.5g$ and a frequency of 2 Hz, outputs with or without friction are negligible and are thus not shown in the figure. The effect of friction is negligible at an excitation acceleration of $1.5g$ and frequencies of 3 Hz–6 Hz. However, the open-circuit P-P voltage is reduced by friction at an excitation acceleration of $1.5g$ and a frequency of 7 Hz. Overall, the effect of friction is smaller at an excitation acceleration of $1.5g$ than that at an excitation acceleration of $1g$. Due to the effect of friction, the excitation point with the maximum response in the figure shifts to the left, indicating a decrease in the excitation frequency at the point of maximum response.

The generators produce large P-P open-circuit voltages at low frequencies, owing to the resonant inter-well oscillations around various local oscillation frequencies at 5 Hz–6 Hz. As the structure and trajectory of the harvester are symmetric, the measurements for EMG1 and EMG2 are similar. As Coil 2 is on the edge of the motion curve, the output P-P value exhibits asymmetry. Coil 1 is closer to the center stable point than Coil 2, and at a higher rate of magnetic induction change, Coil 1 performs better in terms of the output P-P value than Coil 2. When the excitation frequency is set to 2 Hz and 8 Hz, the output is reduced by the inter-well motions of the tip magnet.

The open-circuit P-P voltage outputs of the TENG unit at excitation accelerations of $1g$ and $1.5g$ are presented in Fig. 9(b). As the frequency increases, the output increases until it reaches the point of maximum response. The maximum responses are obtained at an excitation acceleration of $1g$ and a frequency of 5 Hz, and at an excitation acceleration of $1.5g$ and a frequency of 6 Hz. The outputs corresponding to the maximum-response points are 62 V and 80 V, respectively. Figures 9(c) and 9(d) show the friction effect on the open-circuit P-P voltages of the two EMG units with different input signals. The output results of EMG1 indicate that the presence of friction reduces the output and the maximum response frequency. The general trend for EMG2 is similar to that for EMG1, and the observed frictional negative effect of EMG2 is significantly higher than that of EMG1. The output of EMG2 experiences a notable decrease at 7 Hz.

Figure 10 shows the percentages of friction effects for PEG2, EMG1, and EMG2 units at $1g$ and $1.5g$ (with and without friction effects). The results clearly demonstrate that friction can generally reduce the voltage output. EMG1 exhibits the most significant disparity influenced by friction, and all output units under both excitations are more susceptible to its effect. In the analysis, the effect of friction is pronounced at 6 Hz and 7 Hz under $1g$ and $1.5g$, respectively.

To investigate the output performance of the proposed model, the maximum output powers of the TENG, EMG, and PEG units are measured at 5 Hz under $1\,g$ acceleration as shown in Fig. 11. Under the influence of friction, the maximum power for the PEG unit is 48.4 mW across an optimal impedance of approximately 80 kΩ. The maximum power output of the PEG unit is 52 mW (without friction), representing an increase of 7.4% compared with that of the PEG

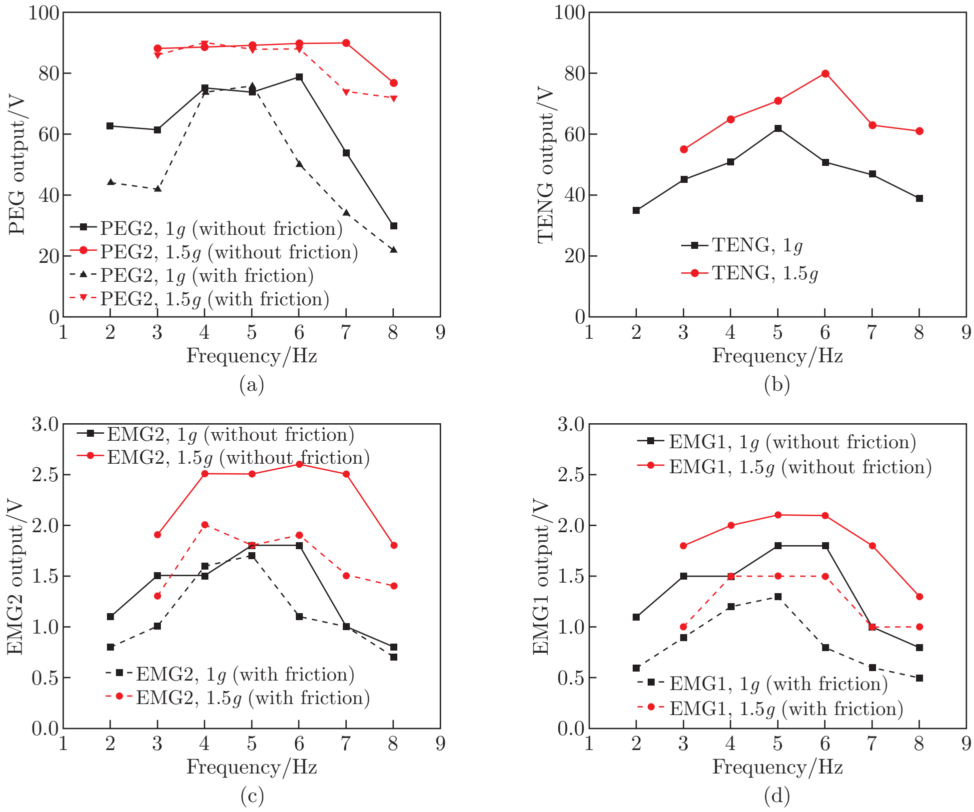

Fig. 9 Open-circuit outputs of different units at excitation accelerations of $1g$ and $1.5g$: (a) PEG2 output (with and without friction effect); (b) TENG output; (c) EMG2 output (with and without friction effect); (d) EMG1 output (with and without friction effect) (color online)

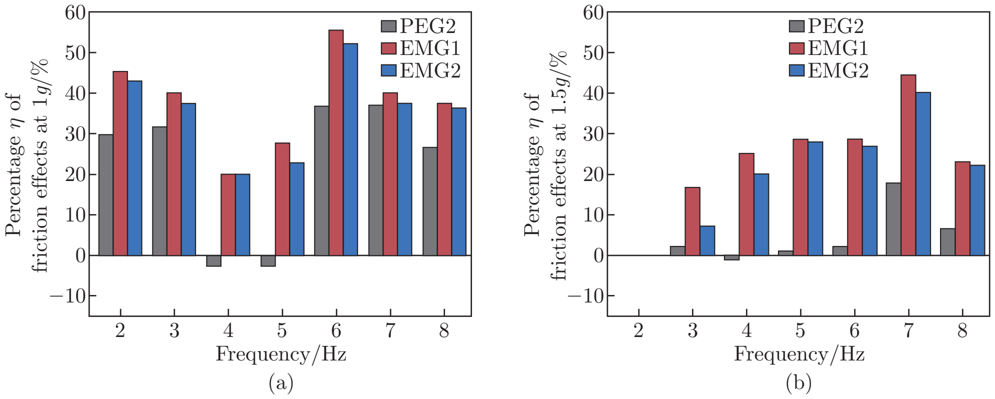

Fig. 10 Percentages of friction effects for PEG2, EMG1, and EMG2 units at $1g$ and $1.5g$ (with and without friction effects): (a) $1g$; (b) $1.5g$, where $\eta = \frac{U_{\mathrm{vol}}-U_{\mathrm{vol,friction}}}{U_{\mathrm{vol}}} \times 100\%$, U_{vol} denotes the voltage output without friction, and $U_{\mathrm{vol,friction}}$ denotes the voltage output with friction (color online)

output with friction. For the EMG unit, we rectify and connect EMG1 and EMG2 units in series to obtain the overall output of EMG. At an impedance of 220 Ω, the maximum EMG output power is 5.87 mW. For the TENG unit, due to its higher internal resistance, the measured optimal matching impedance is 21 MΩ with a maximum power of 51.23 μW. Regardless of the presence of friction, the EMG output remains constant at 5.85 mW and 270 Ω, implying that friction has a negligible impact on the EMG results. The peak power output of the hybrid model (with friction) is 54.26 mW, while the hybrid model (without friction) is 58.75 mW.

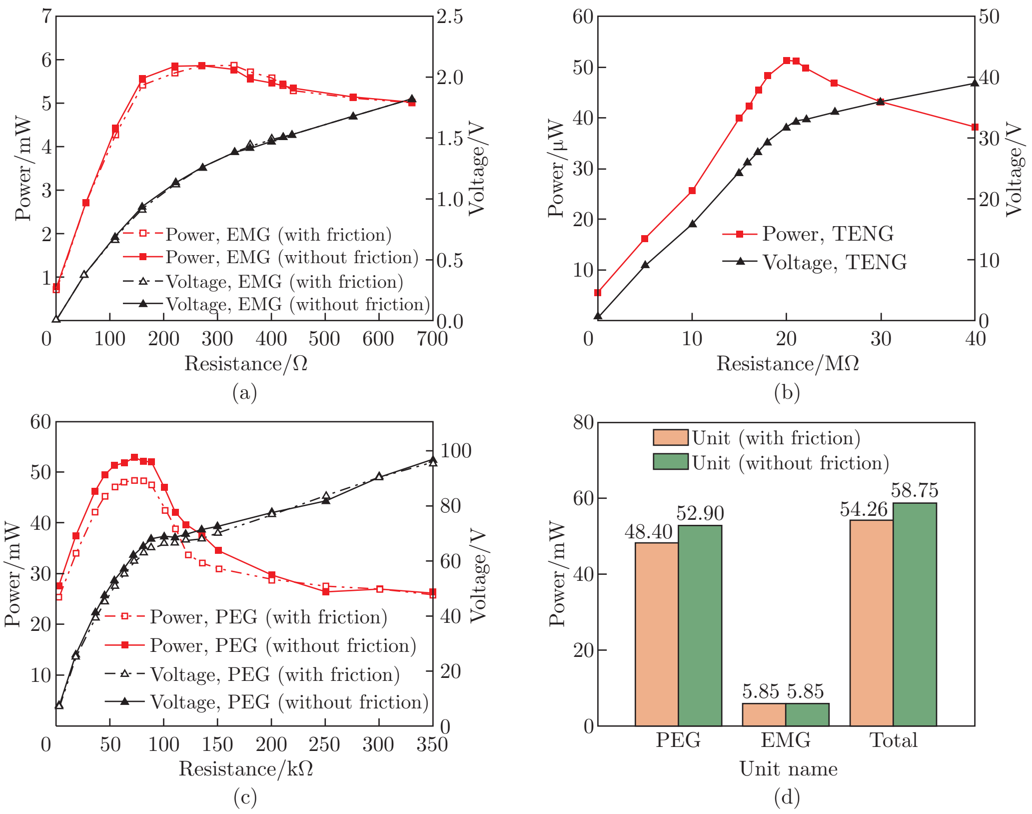

Fig. 11 Performance comparison: (a) EMG unit; (b) TENG unit; (c) PEG unit; (d) EMG, PEG, and total units' output differences, where all results are measured at $1g$ and 5 Hz (color online)

According to the simulation results, it can be observed that the movement of the tip magnet is hindered by frictional force under various excitation signals and coefficients of friction. Experimental findings indicate that frictional force significantly affects the open-circuit output. The output of the designed TENG unit demonstrates notable variations in different experimental environments. To enhance the TENG output, control measures such as temperature regulation, pre-charging techniques, and nano-scale surface treatment of materials can be implemented. This experiment aims to investigate the impact of friction on dynamic motion states; hence, complex friction structures are not employed in this study.

4 Conclusions

We explore a tri-hybrid vibration-based energy harvesting model that has a triboelectric unit operating in sliding mode. We then develop a model for the mechanical vibration of a cantilever beam with a tip mass, which is subject to both magnetic and frictional forces under base excitation. Additionally, we examine the open-circuit P-P voltages of the sliding-mode tri-stable energy harvester. Moreover, dynamic simulations are conducted for different values of μ (0.2–0.5) and initial phases (4 mm and 20 mm). The following findings are obtained based on the effect of the non-conservative force (friction) on the multi-stable system.

(i) Both simulation and experimental results reveal that under most excitations of the cantilever beam structure, friction negatively affects the outputs of PEG unit. At low levels of excitation (e.g., an acceleration of $0.5g$), the frictional force acting within the structure completely impedes the outputs.

(ii) However, friction is not always a negative factor. At a high excitation acceleration, such as $1.5g$, in comparison to the $1g$ excitation, the impact of the friction force is smaller. The TENG unit can achieve a maximum open-circuit voltage output of 80 V and a load power output of 51.23 μW.

(iii) There is a shift in the distribution of multi-stability due to the effect of friction, leading to a decrease in the inter-well motion and a simultaneous increase in the intra-well motion.

(iv) The presence of friction not only diminishes the amplitude of the tip magnet but also reduces the corresponding frequency at which the structure has its maximum-response point. The dynamic characteristics of the model can be significantly influenced by the magnitude of the friction coefficient.

In the absence of frictional influence, the EMG exhibits a maximum output power of 5.85 mW under $1g$ and 5 Hz excitation, while the PEG demonstrates a maximum output power of 52.9 mW. In the presence of frictional effect, the measured output powers of EMG, PEG, and TENG are 5.85 mW, 48.4 mW, and 51.23 μW, respectively.

Conflict of interest The authors declare no conflict of interest.

Acknowledgements The authors thank the found of the Hong Kong Polytechnic University (No. 1-WZ2Z).

References

[1] CARNEIRO, P., SOARES DOS SANTOS, M. P., RODRIGUES, A., FERREIRA, J. A. F., SIMÕES, J. A. O., MARQUES, A. T., and KHOLKIN, A. L. Electromagnetic energy harvesting using magnetic levitation architectures: a review. *Applied Energy*, **260**, 114191 (2020)

[2] BEEBY, S. P. and O'DONNELL, T. Electromagnetic energy harvesting. *Energy Harvesting Technologies*, Springer, New York, 129–161 (2009)

[3] SEZER, N. and KOÇ, M. A comprehensive review on the state-of-the-art of piezoelectric energy harvesting. *Nano Energy*, **80**, 105567 (2021)

[4] KIM, H. S., KIM, J. H., and KIM, J. A review of piezoelectric energy harvesting based on vibration. *International Journal of Precision Engineering and Manufacturing*, **12**, 1129–1141 (2011)

[5] SAFAEI, M., SODANO, H. A., and ANTON, S. R. A review of energy harvesting using piezoelectric materials: state-of-the-art a decade later (2008–2018). *Smart Materials Structures*, **28**, 113001 (2019)

[6] BEEBY, S. P., TUDOR, M. J., and WHITE, N. Energy harvesting vibration sources for microsystems applications. *Measurement Science Technology*, **17**, R175 (2006)

[7] JIN, W., WANG, Z., HUANG, H., HU, X., HE, Y., LI, M., LI, L., GAO, Y., HU, Y., and GU, H. High-performance piezoelectric energy harvesting of vertically aligned Pb(Zr, Ti)O_3 nanorod arrays. *RSC Advances*, **8**, 7422–7427 (2018)

[8] COVACI, C. and GONTEAN, A. Piezoelectric energy harvesting solutions: a review. *Sensors*, **20**, 3512 (2020)

[9] DAI, X., WANG, H., WU, H., PAN, Y., LUO, D., AHMED, A., and ZHANG, Z. A hybrid energy harvesting system for self-powered applications in shared bicycles. *Sustainable Energy Technologies and Assessments*, **51**, 101891 (2022)

[10] SIANG, J., LIM, M. H., and LEONG, M. S. Review of vibration-based energy harvesting technology: mechanism and architectural approach. *International Journal of Energy Research*, **42**, 1866–1893 (2018)

[11] YANG, B., XUAN, F. Z., JIN, P., HU, C., XIAO, B., LI, D., XIANG, Y., and LEI, H. Damage localization in composite laminates by building in PZT wafer transducers: a comparative study with surface-bonded PZT strategy. *Advanced Engineering Materials*, **21**, 1801040 (2019)

[12] MARZENCKI, M., BASROUR, S., CHARLOT, B., GRASSO, A., COLIN, M., and VALBIN, L. Design and fabrication of piezoelectric micro power generators for autonomous microsystems. *Proceedings of Symposium on Design*, *Test*, *Integration and Packaging of MEMS/MOEMS*, Switzerland, 299–302 (2005)

[13] ROGACHEVA, N. N. The dynamic behaviour of piezoelectric laminated bars. *Journal of Applied Mathematics and Mechanics*, **71**, 494–510 (2007)

[14] SHAO, N., CHEN, Z., WANG, X., ZHANG, C., XU, J., XU, X., and YAN, R. Modeling and analysis of magnetically coupled piezoelectric dual beam with an annular potential energy function for broadband vibration energy harvesting. *Nonlinear Dynamics*, **111**, 11911–11937 (2023)

[15] DAI, H. L., ABDELMOULA, H., ABDELKEFI, A., and WANG, L. Towards control of cross-flow-induced vibrations based on energy harvesting. *Nonlinear Dynamics*, **88**, 2329–2346 (2017)

[16] LI, H. and QIN, W. Dynamics and coherence resonance of a laminated piezoelectric beam for energy harvesting. *Nonlinear Dynamics*, **81**, 1751–1757 (2015)

[17] CHEN, L. Q. and FAN, Y. Internal resonance vibration-based energy harvesting. *Nonlinear Dynamics*, **111**, 11703–11727 (2023)

[18] LI, M., YU, D., LI, Y., LIU, X., and DAI, F. Integrated a nonlinear energy sink and a piezoelectric energy harvester using simply-supported bi-stable piezoelectric composite laminate. *International Journal of Non-Linear Mechanics*, **156**, 104464 (2023)

[19] FAN, Y., GHAYESH, M. H., LU, T. F., and AMABILI, M. Design, development, and theoretical and experimental tests of a nonlinear energy harvester via piezoelectric arrays and motion limiters. *International Journal of Non-Linear Mechanics*, **142**, 103974 (2022)

[20] SU, M., XU, W., and ZHANG, Y. Theoretical analysis of piezoelectric energy harvesting system with impact under random excitation. *International Journal of Non-Linear Mechanics*, **119**, 103322 (2020)

[21] ESHTEHARDIHA, R., TIKANI, R., and ZIAEI RAD, S. Experimental and numerical investigation of energy harvesting from double cantilever beams with internal resonance. *Journal of Sound and Vibration*, **500**, 116022 (2021)

[22] SARKER, M. R., SAAD, M. H. M., OLAZAGOITIA, J. L., and VINOLAS, J. Review of power converter impact of electromagnetic energy harvesting circuits and devices for autonomous sensor applications. *Electronics*, **10**, 1108 (2021)

[23] FU, H., THEODOSSIADES, S., GUNN, B., ABDALLAH, I., and CHATZI, E. Ultra-low frequency energy harvesting using bi-stability and rotary-translational motion in a magnet-tethered oscillator. *Nonlinear Dynamics*, **101**, 2131–2143 (2020)

[24] FAN, F. R., TIAN, Z. Q., and WANG, Z. L. Flexible triboelectric generator. *Nano Energy*, **1**, 328–334 (2012)

[25] JIN, C., KIA, D. S., JONES, M., and TOWFIGHIAN, S. On the contact behavior of micro-/nano-structured interface used in vertical-contact-mode triboelectric nanogenerators. *Nano Energy*, **27**, 68–77 (2016)

[26] SHIN, S. H., KWON, Y. H., KIM, Y. H., JUNG, J. Y., LEE, M. H., and NAH, J. Triboelectric charging sequence induced by surface functionalization as a method to fabricate high performance triboelectric generators. *ACS Nano*, **9**, 4621–4627 (2015)

[27] HE, X., GUO, H., YUE, X., GAO, J., XI, Y., and HU, C. Improving energy conversion efficiency for triboelectric nanogenerator with capacitor structure by maximizing surface charge density. *Nanoscale*, **7**, 1896–1903 (2015)

[28] BUSOLO, T., URA, D. P., KIM, S. K., MARZEC, M. M., BERNASIK, A., STACHEWICZ, U., and KAR NARAYAN, S. Surface potential tailoring of PMMA fibers by electrospinning for enhanced triboelectric performance. *Nano Energy*, **57**, 500–506 (2019)

[29] LIU, H., FU, H., SUN, L., LEE, C., and YEATMAN, E. M. Hybrid energy harvesting technology: from materials, structural design, system integration to applications. *Renewable and Sustainable Energy Reviews*, **137**, 110473 (2021)

[30] BOLAT, F. C., BASARAN, S., and SIVRIOGLU, S. Piezoelectric and electromagnetic hybrid energy harvesting with low-frequency vibrations of an aerodynamic profile under the air effect. *Mechanical Systems and Signal Processing*, **133**, 106246 (2019)

[31] YANG, X., LAI, S. K., WANG, C., WANG, J. M., and DING, H. On a spring-assisted multi-stable hybrid-integrated vibration energy harvester for ultra-low-frequency excitations. *Energy*, **252**, 124028 (2022)

[32] CHEN, K., GAO, Q., FANG, S., ZOU, D., YANG, Z., and LIAO, W. H. An auxetic nonlinear piezoelectric energy harvester for enhancing efficiency and bandwidth. *Applied Energy*, **298**, 117274 (2021)

[33] WANG, C., LAI, S. K., WANG, J. M., FENG, J. J., and NI, Y. Q. An ultra-low-frequency, broadband and multi-stable tri-hybrid energy harvester for enabling the next-generation sustainable power. *Applied Energy*, **291**, 116825 (2021)

[34] ZHAO, L. C., ZOU, H. X., ZHAO, Y. J., WU, Z. Y., LIU, F. R., WEI, K. X., and ZHANG, W. M. Hybrid energy harvesting for self-powered rotor condition monitoring using maximal utilization strategy in structural space and operation process. *Applied Energy*, **314**, 118983 (2022)

[35] WANG, C., JI, Y., LAI, S. K., LIU, Y., HAO, Y., LI, G., WANG, C., and WEN, G. L. A speed-amplified tri-stable piezoelectric-electromagnetic-triboelectric hybrid energy harvester for low-frequency applications. *Nano Energy*, **114**, 108630 (2023)

[36] CHEN, H. Y., ZENG, Y. C., DING, H., LAI, S. K., and CHEN, L. Q. Dynamics and vibration reduction performance of asymmetric tristable nonlinear energy sink. *Applied Mathematics and Mechanics (English Edition)*, **45**, 389–406 (2024) https://doi.org/10.1007/s10483-024-3095-9

[37] ZHOU, S., LALLART, M., and ERTURK, A. Multistable vibration energy harvesters: principle, progress, and perspectives. *Journal of Sound and Vibration*, **528**, 116886 (2022)

[38] HE, X., WEN, Q., SUN, Y., and WEN, Z. A low-frequency piezoelectric-electromagnetic-triboelectric hybrid broadband vibration energy harvester. *Nano Energy*, **40**, 300–307 (2017)

[39] WANG, C., LAI, S. K., WANG, Z. C., WANG, J. M., YANG, W., and NI, Y. Q. A low-frequency, broadband and tri-hybrid energy harvester with septuple-stable nonlinearity-enhanced mechanical frequency up-conversion mechanism for powering portable electronics. *Nano Energy*, **64**, 103943 (2019)

[40] CHENG, T., GAO, Q., and WANG, Z. L. The current development and future outlook of triboelectric nanogenerators: a survey of literature. *Advanced Materials Technologies*, **4**, 1800588 (2019)

[41] SONG, C., ZHU, X., WANG, M., YANG, P., CHEN, L., HONG, L., and CUI, W. Recent advances in ocean energy harvesting based on triboelectric nanogenerators. *Sustainable Energy Technologies and Assessments*, **53**, 102767 (2022)

[42] LIN, Z. H., ZHU, G., ZHOU, Y. S., YANG, Y., BAI, P., CHEN, J., and WANG, Z. L. A self-powered triboelectric nanosensor for mercury ion detection. *Angewandte Chemie*, **125**, 5169–5173 (2013)

[43] WARDHANA, E. M., MUTSUDA, H., TANAKA, Y., NAKASHIMA, T., KANEHIRA, T., MAEDA, S., and YAMAUCHI, M. Characteristics of electric performance and key factors of a hybrid piezo/triboelectric generator for wave energy harvesting. *Sustainable Energy Technologies and Assessments*, **50**, 101757 (2022)

[44] WANG, S., LIN, L., XIE, Y., JING, Q., NIU, S., and WANG, Z. L. Sliding-triboelectric nanogenerators based on in-plane charge-separation mechanism. *Nano Letters*, **13**, 2226–2233 (2013)

[45] LIN, Z., WU, Z., ZHANG, B., WANG, Y. C., GUO, H., LIU, G., CHEN, C., CHEN, Y., YANG, J., and WANG, Z. L. A triboelectric nanogenerator-based smart insole for multifunctional gait monitoring. *Advanced Materials Technologies*, **4**, 1800360 (2019)

[46] LI, J., CHENG, L., WAN, N., MA, J., HU, Y., and WEN, J. Hybrid harvesting of wind and wave energy based on triboelectric-piezoelectric nanogenerators. *Sustainable Energy Technologies and Assessments*, **60**, 103466 (2023)

[47] YANG, Y., ZHANG, H., CHEN, J., JING, Q., ZHOU, Y. S., WEN, X., and WANG, Z. L. Single-electrode-based sliding triboelectric nanogenerator for self-powered displacement vector sensor system. *ACS Nano*, **7**, 7342–7351 (2013)

[48] WANG, S., XIE, Y., NIU, S., LIN, L., and WANG, Z. L. Freestanding triboelectric-layer-based nanogenerators for harvesting energy from a moving object or human motion in contact and non-contact modes. *Advanced Materials*, **26**, 2818–2824 (2014)

[49] WANG, Z. L. Triboelectric nanogenerators as new energy technology for self-powered systems and as active mechanical and chemical sensors. *ACS Nano*, **7**, 9533–9557 (2013)

[50] KARAPETYAN, A. V. Modelling of frictional forces in the dynamics of a sphere on a plane. *Journal of Applied Mathematics and Mechanics*, **74**, 380–383 (2010)

[51] MU, J., ZOU, J., SONG, J., HE, J., HOU, X., YU, J., HAN, X., FENG, C., HE, H., and CHOU, X. Hybrid enhancement effect of structural and material properties of the triboelectric generator on its performance in integrated energy harvester. *Energy Conversion and Management*, **254**, 115151 (2022)

[52] CHANDRASEKARAN, S., BOWEN, C., ROSCOW, J., ZHANG, Y., DANG, D. K., KIM, E. J., MISRA, R. D. K., DENG, L., CHUNG, J. S., and HUR, S. H. Micro-scale to nano-scale generators for energy harvesting: self powered piezoelectric, triboelectric and hybrid devices. *Physics Reports*, **792**, 1–33 (2019)

[53] TAN, D., ZHOU, J., WANG, K., CAI, C., and XU, D. Modeling and analysis of the friction in a nonlinear sliding-mode triboelectric energy harvester. *Acta Mechanica Sinica*, **38**, 521330 (2022)

[54] FU, Y., OUYANG, H., and DAVIS, R. B. Effects of electrical properties on vibrations via electromechanical coupling in triboelectric energy harvesting. *Journal of Physics D: Applied Physics*, **53**, 215501 (2020)

[55] FU, Y., OUYANG, H., and BENJAMIN DAVIS, R. Nonlinear structural dynamics of a new sliding-mode triboelectric energy harvester with multistability. *Nonlinear Dynamics*, **100**, 1941–1962 (2020)

[56] PAN, D., FAN, B., QI, X., YANG, Y., and HAO, X. Investigation of PTFE tribological properties using molecular dynamics simulation. *Tribology Letters*, **67**, 28 (2019)

[57] BISWAS, S. K. and VIJAYAN, K. Friction and wear of PTFE — a review. *Wear*, **158**, 193–211 (1992)

[58] UNAL, H., MIMAROGLU, A., KADIOGLU, U., and EKIZ, H. Sliding friction and wear behaviour of polytetrafluoroethylene and its composites under dry conditions. *Materials & Design*, **25**, 239–245 (2004)

[59] ZOBOVA, A. A. A review of models of distributed dry friction. *Journal of Applied Mathematics and Mechanics*, **80**, 141–148 (2016)

[60] ZIEGLER, F. D'Alembert's principle and Lagrange equations of motion. *Mechanics of Solids and Fluids*, Springer, New York, 565–590 (1995)

[61] FANG, H. and WANG, K. W. Piezoelectric vibration-driven locomotion systems — exploiting resonance and bistable dynamics. *Journal of Sound and Vibration*, **391**, 153–169 (2017)

[62] LENG, Y., TAN, D., LIU, J., ZHANG, Y., and FAN, S. Magnetic force analysis and performance of a tri-stable piezoelectric energy harvester under random excitation. *Journal of Sound and Vibration*, **406**, 146–160 (2017)

[63] AGASHE, J. S. and ARNOLD, D. P. A study of scaling and geometry effects on the forces between cuboidal and cylindrical magnets using analytical force solutions. *Journal of Physics D: Applied Physics*, **41**, 105001 (2008)